aerospace

MDPI

Article

ARC-LIGHT: Algorithm for Robust Characterization of Lunar Surface Imaging for Ground Hazards and Trajectory

Alexander Cushen [1,*], Ariana Bueno [1,*], Samuel Carrico [2], Corrydon Wettstein [3], Jaykumar Ishvarbhai Adalja [1], Mengxiang Shi [3], Naila Garcia [4], Yuliana Garcia [4], Mirko Gamba [2] and Christopher Ruf [1]

[1] Climate and Space Sciences and Engineering Department, University of Michigan, Ann Arbor, MI 48109, USA; jadalja@umich.edu (J.I.A.); cruf@umich.edu (C.R.)
[2] Department of Aerospace Engineering, University of Michigan, Ann Arbor, MI 48109, USA; samcarr@umich.edu (S.C.); mirkog@umich.edu (M.G.)
[3] Electrical Engineering and Computer Science Department, University of Michigan, Ann Arbor, MI 48109, USA; cordymw@umich.edu (C.W.); mengxshi@umich.edu (M.S.)
[4] Department of Mechanical Engineering, University of Michigan, Ann Arbor, MI 48109, USA; garnaila@umich.edu (N.G.); yulianag@umich.edu (Y.G.)
* Correspondence: atcushen@umich.edu (A.C.); aribueno@umich.edu (A.B.)

Abstract: Safe and reliable lunar landings are crucial for future exploration of the Moon. The regolith ejected by a lander's rocket exhaust plume represents a significant obstacle in achieving this goal. It prevents spacecraft from reliably utilizing their navigation sensors to monitor their trajectory and spot emerging surface hazards as they near the surface. As part of NASA's 2024 Human Lander Challenge (HuLC), the team at the University of Michigan developed an innovative concept to help mitigate this issue. We developed and implemented a machine learning (ML)-based sensor fusion system, ARC-LIGHT, that integrates sensor data from the cameras, lidars, or radars that landers already carry but disable during the final landing phase. Using these data streams, ARC-LIGHT will remove erroneous signals and recover a useful detection of the surface features to then be used by the spacecraft to correct its descent profile. It also offers a layer of redundancy for other key sensors, like inertial measurement units. The feasibility of this technology was validated through development of a prototype algorithm, which was trained on data from a purpose-built testbed that simulates imaging through a dusty environment. Based on these findings, a development timeline, risk analysis, and budget for ARC-LIGHT to be deployed on a lunar landing was created.

Keywords: Plume Surface Interaction (PSI); lunar; landing; navigation; machine learning; Artemis; dust; imaging; algorithm; surface hazards

check for updates

Academic Editor: Marco Sabatini

Received: 14 January 2025
Revised: 7 February 2025
Accepted: 22 February 2025
Published: 24 February 2025

Citation: Cushen, A.; Bueno, A.; Carrico, S.; Wettstein, C.; Adalja, J.I.; Shi, M.; Garcia, N.; Garcia, Y.; Gamba, M.; Ruf, C. ARC-LIGHT: Algorithm for Robust Characterization of Lunar Surface Imaging for Ground Hazards and Trajectory. *Aerospace* **2025**, *12*, 177. https://doi.org/10.3390/aerospace12030177

Copyright: © 2025 by the authors. Licensee MDPI, Basel, Switzerland. This article is an open access article distributed under the terms and conditions of the Creative Commons Attribution (CC BY) license (https://creativecommons.org/licenses/by/4.0/).

1. Introduction

1.1. Problem Statement

As international interest in lunar science and exploration grows, the capability for safe and precise landings on the Moon's surface has become more important than ever. Recent missions like SLIM, Chang'e, IM-1, and Chandrayaan have made major strides in this field, but NASA's ambitious Artemis program, which aims to provide regular access to the surface for crew and cargo, necessitate enhanced reliability and accuracy of lunar landings. A significant hazard during these landings is the ejection of regolith as a lander's rocket plume impinges on the surface. This Plume Surface Interaction (PSI) results from the engine exhaust of a lander interacting with the surface of a planetary body during the landing

and ascent phases. PSI can eject large amounts of regolith particles that can limit visibility, spoof navigation systems, and damage surrounding surface assets. Understanding and mitigating challenges due to PSI is paramount for the safety and success of upcoming lunar missions. Therefore, NASA developed the first Human Lander Challenge (HuLC) in 2024, an initiative supporting NASA's Exploration Systems Development Mission Directorate (ESDMD) efforts to explore innovative solutions for a variety of known Human Landing System (HLS) challenge areas, including PSI. The team at the University of Michigan was formed to design an innovative solution that would address the mitigation of lunar PSI.

A significant challenge presented by PSI is dust interference with navigation systems; the lofted clouds of regolith can obstruct the view of the cameras, radars, and lidars used for navigation. During the Apollo landings, astronauts observed various instances where PSI was responsible for visual limitations and radar interference during landing, most notably in Apollo 15 [1]. Current lunar missions typically employ cameras for computer vision-based optical navigation and lidar and radar systems to model surface features and determine their state vector, their position, and attitude relative to surface landmarks. As landers near the surface, these systems are continuously affected by the regolith lofted by PSI. The PSI-induced dust clouds obscure the view of the surface, change the ambient lighting conditions, and provide a diffuse reflective surface for lidar and radar signals to bounce off. As such, contemporary lunar landers like Chang'e typically do not use these sensors during the final stage of vertical descent due to PSI-induced dust interference [2].

To address this issue, we proposed a machine learning (ML)-based sensor fusion system that integrates sensor data from standard navigation sensors to be effectively utilized during the final descent phase of landing. The Algorithm for Robust Characterization of Lunar surface Imaging for Ground Hazards and Trajectory (ARC-LIGHT) fuses measurements from cameras, lidars, or other employed sensors to remove signal noise and allow the spacecraft to "see through" the PSI cloud. This, in turn, will enhance landing accuracy by allowing for recalibration of the state vector during vertical descent and improve landing safety by enabling hazard avoidance scans at lower altitudes. Since the system employs data from sensors already on the spacecraft, ARC-LIGHT will not add any hardware mass or complexity to the landers and is readily compatible with multiple lander types.

To demonstrate the feasibility of this technology, we established a test bed facility to gather sensor data affected by a diffuse optically scattering medium. The dataset from this experiment was used to demonstrate a prototype sensor fusion algorithm for reconstructing lidar scans. These results informed the proposed timeline, project risk management strategy, and a draft budget for the development and deployment of ARC-LIGHT for future lunar missions, as presented in Appendix A.

1.2. Background

Modern lunar landers rely on autonomous systems to safely conduct entry, landing, and descent (EDL) on the Moon. These landers often rely on lidar or radar altimeters and velocimeters, inertial measurement units (IMUs), star trackers, and vision-based methods to properly locate themselves during descent. They also combine two-dimensional image-based methods with three-dimensional lidar readings to locate and avoid hazards [3]. These sensors are enabled and disabled as needed during different phases of descent.

The recent robotic landings of Chang'e 3–6, Chandrayaan-3, IM-1, and SLIM each employ a similar EDL profile, illustrated in Figure 1 [2,4–6]. Following descent orbit insertion, the lander begins powered descent around 20 km above the surface. Powered descent consists of three phases: braking, approach, and vertical descent. The braking phase serves to reduce the lander's velocity from orbital speeds. A star tracker and IMU remain active throughout this phase, with lidar altimeters and velocimeters activated

around 10 km. These serve to update the state vector as it evolves from the initial orbital parameters. During the approach phase, ranging from around 5 km to 100 m above the lunar surface, the lander establishes visual contact with the landing ellipse. The star tracker, IMU, altimeters, and velocimeters remain active, with an optical camera also activated during this phase. Finally, the vertical descent phase occurs, preceded by a hazard detection and avoidance (HDA) scan at 50–100 m above the surface, which uses a lidar to determine a safe landing site. Local landmarks are used to provide a local reference frame, called terrain relative navigation (TRN) [5]. The lander continues using sensors as it navigates to a position approximately 50 m above the selected landing site. Below this altitude, it disables every sensor except for its IMU for final vertical descent [4]. Exceptionally, the recent Chang'e-6 lander made use of a gamma ray detector to independently ascertain its altitude, even when optical interference due to PSI was significant, but such instruments are not standard inclusions for other contemporary landers, given their weight and power demands [7].

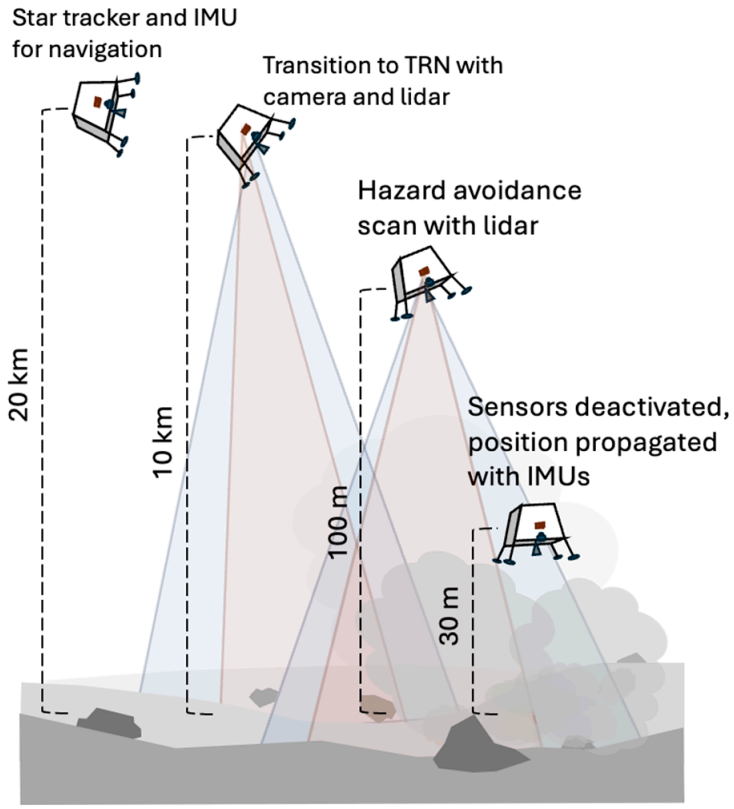


Figure 1. General framework for sensor usage during EDL, showing navigation methodology at different stages, including deactivation for vertical descent.

A significant reason for autonomous landers disabling their sensors during final descent is the effect of PSI. The high density of dust particles ejected during landing can interfere with the sensors, causing them to be unreliable. The Chang'e 3 mission observed this interference 20 m above the lunar surface during its landing [2], but PSI onset at higher altitudes has been observed for higher thrust landers [8,9]. The general lack of active sensor guidance during this period of the flight increases the possibility of error, potentially leading to catastrophic consequences for the spacecraft.

2. Technology Concept and Innovation

2.1. Objectives

To improve lunar landing accuracy and safety, we proposed a sensor fusion-based navigation algorithm, ARC-LIGHT, which takes advantage of otherwise unused sensor data during the final stage of vertical descent. ARC-LIGHT is motivated by three key objectives:

1. Improve landing accuracy within the landing zone by allowing for recalibration of the spacecraft vector using TRN during vertical descent;
2. Improve hazard detection by enabling hazard avoidance scans at lower altitudes to spot small surface features that could not be seen from higher altitudes and pits or rocks moved or formed by PSI;
3. Provide sensor redundancy in the case of IMU failure during landing.

ARC-LIGHT fulfills these objectives by deploying a number of sensor fusion signal processing techniques, namely a convolutional neural network (CNN), to integrate multiple data streams and reconstruct a clear lidar scan of the surface. This machine learning-based framework is flexible and lander-agnostic, easily adjusting to take advantage of different sensor configurations, including lidars, cameras, and radars. With ARC-LIGHT, the spacecraft will be able to "see through" the PSI cloud, providing an additional layer of navigational redundancy during the crucial terminal landing phase. This technology represents a novel application for emerging sensor fusion techniques.

2.2. Sensor Fusion Algorithm

ARC-LIGHT uses sensor fusion, which is the signal processing framework of combining separate sensor datasets into an integrated data product to provide greater measurement confidence and precision [10]. This technique is most useful where multiple sensor types (e.g., cameras and lidars) observe a scene simultaneously; lidars offer 3D structure information, while cameras provide a broader contextualization of the scene. Since each sensor responds to signal interference differently, the combination of their encoded information allows for a clearer signal to be extracted. Recent research has demonstrated the efficacy of this combination for both terrestrial autonomous navigation [11] and dust de-filtering [12].

Multiple sensor fusion techniques may be applied to help improve the spacecraft's lidar and camera observations during vertical descent. The choice of which techniques to implement depends on the sensor availability and configuration on the spacecraft, as well as computational resources and landing precision requirements. Figure 2 outlines the proposed architecture for ARC-LIGHT, demonstrating how multiple techniques may be combined. As lidar-camera fusion is an emerging technology, there are few established algorithmic conventions to compare to; the separate pre-processing pathways before CNN-based fusion are comparable to other proposed architectures for dust filtering [12], but the comparison to previous iteration outputs is a unique processing stage that takes advantage of the known physics of the spacecraft descent geometry. CNNs are selected at present for their flexibility and simplicity of implementation, but future refinement of this algorithm, including the use of more specialized neural network architectures, will be informed by trade studies and mission requirements for computational cost and performance metrics.

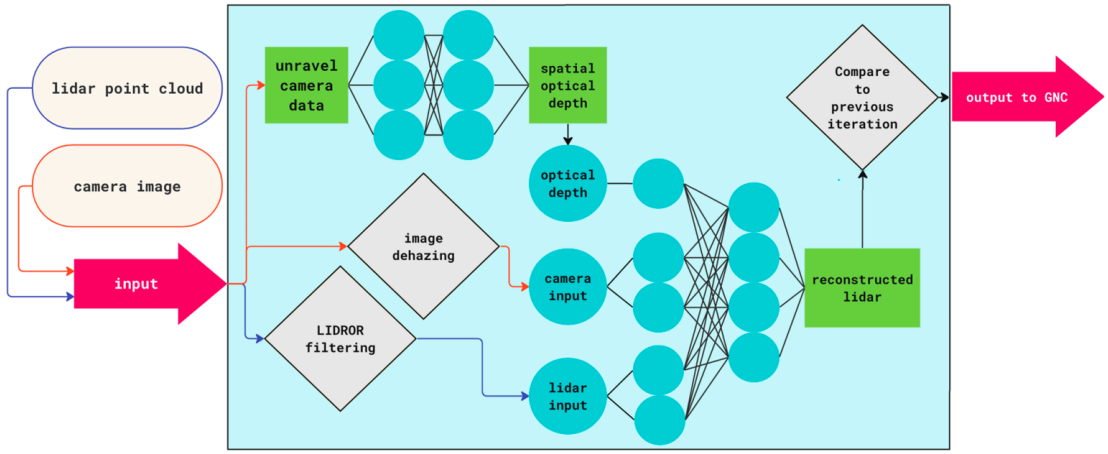


Figure 2. Prototype algorithm architecture; the blue box represents new data processing steps introduced by ARC-LIGHT between sensor readings and spacecraft GNC. Lidar and camera data are input. Image data is processed in initial CNN to determine optical depth of the image in multiple sectors and dehazed to improve signal-to-noise. Lidar data is filtered to remove significant outliers corresponding to strong PSI cloud backscatter. These intermediate quantities are combined in a second CNN to reconstruct the lidar scan without interference. Output is sent to GNC.

In this proposed algorithm, a LIDROR-type filter [13] is first applied to the lidar input to remove lidar points with low local intensity, corresponding to stochastic cloud backscatter. This form of backscatter is caused by strong reflection from lofted regolith particles. The camera data is fed into a CNN, which estimates the optical depth of the lofted regolith in different sectors of the image (e.g., a 16 × 16 grid) to accommodate spatial inhomogeneity of the PSI cloud, allowing for the lidar data from each region to be processed according to the local dust density. The division of the visual field into different sectors has demonstrated success in similar dust detection algorithms [12]. The optical depth τ is a dimensionless measure of light extinction, which is related to the number density of lofted regolith n, regolith cross-section σ, and light path length s:

$$\tau = n\sigma s \tag{1}$$

The image data is also fed into a dehazing module, which increases signal-to-noise for better identification of surface features. Dehazing is an image processing formula that aims to remove haze or blurriness from an image. One common dehazing algorithm is dark channel prior (DCP). DCP uses pixels with low intensity in one of the RGB channels; these pixels are deemed the "dark pixels". It should be noted that spacecraft navigation cameras may be monochromatic. However, even if there are no RGB channels, DCP is still feasible since the algorithm runs by channel; therefore, it would only exercise through the one available channel. It is one of the fastest dehazing algorithms, and its light computational cost is ideal for a resource-constrained lunar lander.

The optical depth estimate, dehazed image, and filtered lidar data are then fed into a second CNN, which integrates these data streams to re-create the lidar scan of the surface as if no PSI were present. This reconstructed lidar scan is then compared to previous iterations to detect any significant errors. If output error exceeds operational bounds due to excessive PSI interference levels, ARC-LIGHT is automatically deactivated. The flexibility of CNNs allows the output to mimic the existing lidar data format used at earlier stages of the descent, removing the need for additional data reprocessing by the lander's GNC. Assuming the output is within bounds, the lidar reconstruction is sent to the GNC in this native lidar format for immediate use at a target 1 Hz cadence. This cadence is

subject to computational cost and precision requirements of the mission but is feasible to achieve given the low computational cost of using trained CNNs. Heuristics strategies may also help to improve computational efficiency. These are techniques to constrain the decision-making processes and choose optimal solutions without expending unnecessary computational resources trying to find a mathematically perfect one [14].

2.3. Operation

Currently, landers accomplish vertical descent by integrating their position based on IMU measurements. This leaves them essentially blind as they are unable to rely on optical sensors like lidar to confirm their location. This results in growing positional uncertainty as to where the lander is located relative to where it believes it is. From the Chang'e 3 and Chang'e 5 missions, positional uncertainty of $\Delta x \approx 2$ m was observed [2,4]. This position uncertainty is partially due to the combined effects of error in state vector determination during EDL and the steady impact of IMU drift between state vector calibration. Given the constant error present in any IMU, the integrated error in acceleration and rotation results in a positional uncertainty [15]:

$$\Delta x = vt\sin\left(\frac{ARW}{60}\sqrt{t}\right) + vt\sin\left(\frac{BI}{3600}t\right) \quad (2)$$

where v is the lander velocity and t is time since calibration. ARW represents the IMU's angle random walk, which is the random noise error of an IMU's gyroscopes. BI represents the IMU's bias instability, which is the drift the IMU's measurements have from the average value of its output rate. For this calculation, we used the parameters from the Chang'e 5 landing, a velocity of 1.5 m/s and a descent time of 66.66 s, and a commercial IMU, with a BI of 0.25 degrees/hour and an ARW of 0.125 degree/$\sqrt{\text{hour}}$ [4,16]. In this case, the positional uncertainty caused by IMU drift is only approximately 4 cm, which is very small compared to the total uncertainty of approximately 2 m. We can conclude that the vast majority of a lander's positional uncertainty is caused by other forms of error, such as error in the initial HDA scan or environmental effects. ARC-LIGHT can combat these difficult-to-quantify errors through constant recalibration of the lander's position.

ARC-LIGHT provides the lander with the synthesized altitude data to make periodic recalibrations of the state vector throughout vertical descent to account for any drift, as illustrated in Figure 3. This state vector correction will be performed by the GNC with the same software already used during earlier descent stages. This is done using an extended Kalman filter that combines observational data with the propagated position estimate, accounting for the computational delay of processing surface observation data [5,17].

Beyond its ability to increase the precision of a lunar lander, ARC-LIGHT will also allow the lander to detect changes in the surface, which include hazards uncovered by PSI, or features that are too small to resolve at the initial HDA scan height. The reconstructed lidar scan can be used to assess the magnitude of these hazards and perform course corrections if needed. ARC-LIGHT also provides redundancy in case the IMU were to fail, as it could help the lander calculate its inertial measurements based off the images taken. All of these benefits of ARC-LIGHT will help landers execute safer and more accurate landings on the Moon.

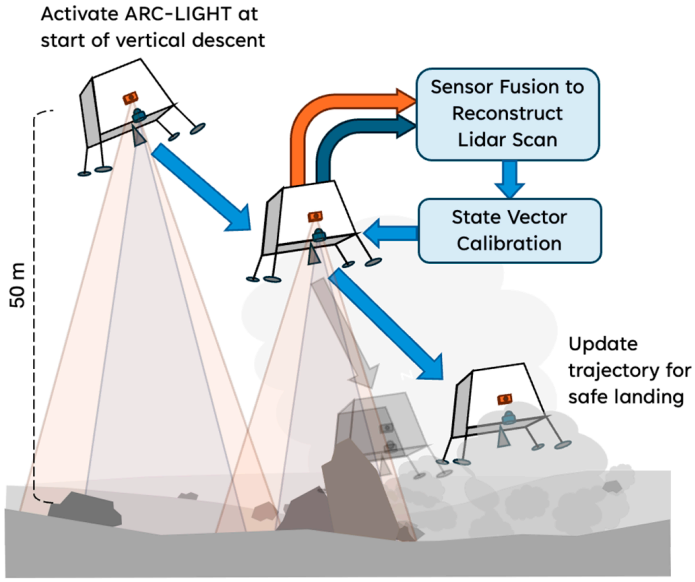


Figure 3. Illustration of final descent where ARC-LIGHT is used to update spacecraft trajectory.

2.4. Training and Verification Plan

Large amounts of lunar lander data will be needed to train and test the algorithm before operational use. It is infeasible to provide a large enough amount of data solely from available lunar landings given how few have occurred. Ground testing will be employed to supplement these few real-world cases, but cost and time limitations limit the number of experimental runs that can be performed. Additionally, in a lunar test bed, it is infeasible to control all experimental factors, such as lighting, vacuum conditions, scale, and gravitational conditions, to accurately reproduce a lunar landing. Given these limitations, we prototyped the algorithm using initial test bed data, and future work will include pre-training our network using synthetic data generated from computational PSI simulations.

PSI models can simulate various scenarios with precise control across a broad parameter space, including particle size and density, surface bonding force, and lander descent profiles [18–20]. They have been developed using various methods to re-create the interaction between rocket plumes and regolith particles in the lunar environment [21–24]. For instance, the Direct Simulation Monte Carlo (DSMC) method simulates the behavior of lunar regolith ejecta generated by PSI on a kinetic level by computing individual macroparticle trajectories, including stochastic collisions, and resolving time-accurate details like density, velocity, and particle size distribution.

These time-resolved datasets provide the basic data needed to generate the needed training data for ARC-LIGHT. Using both high-fidelity optical simulation and 3D modeling tools like Blender, the regolith dust distribution can be translated into synthetic images simulating what a lander would observe during a landing. Further, Mie scattering calculations allow for accurate lidar backscatter simulations, providing the associated lidar data alongside the camera images. Test bed experiments with regolith simulant will help calibrate these optical simulations. While any given simulation and sensor reconstruction is unlikely to mimic reality perfectly, the broad parameter space captured in this synthetic data encompasses the conceivable range of conditions the CNN may face on the Moon.

By pre-training the CNN on a broad training dataset, the need for real-world data is drastically reduced. This approach has demonstrated success for CNN object prediction based on synthetic image-based training [25,26]. The CNN developed from this training can then be fine-tuned using the limited high-fidelity test bed data and currently available sensor data from lunar landings [27,28]. Fine-tuning is a training technique to refine the

accuracy of a pre-trained CNN toward the specific use case by performing small training steps on real-world data.

To ensure the safety of the mission and validate the success of ARC-LIGHT, error quantification will provide a baseline to establish shutoff protocols. ARC-LIGHT will be set to deactivate once PSI becomes significant enough that reliable outputs can no longer be guaranteed. This cutoff point can be determined from an initial hazard scan. Once the standard error is calculated, we could program the system to shut off ARC-LIGHT if the distance measured is more than one standard deviation from the initial scan. Additionally, ARC-LIGHT can be verified as a passive system during an initial lunar lander mission to test out the system, collect data, and build confidence in the pre-training approach. Since ARC-LIGHT does not add additional hardware, implementing this verification step will not require a lot of additional computational cost or added risk to the mission since it will be incorporated as a passive system to be tested.

3. Feasibility Analysis

To fulfill its objectives of improving landing accuracy, safety, and redundancy, ARC-LIGHT calls for the development of ML systems that are robust to the optical interference of the PSI landing environment. To assess the feasibility of this concept, we have undertaken an experimental campaign to study the response of lidars and cameras to a simulated lunar environment and develop a prototype ML-based sensor fusion algorithm for lidar reconstruction. This section reviews the present operational uses of ML-based navigation in spaceflight, introduces our experimental facility and prototype algorithm, and presents our findings from this study.

3.1. Review of Machine Learning in Spacecraft Navigation

Sensor fusion and ML-based navigation systems have a demonstrated heritage in autonomous vehicles [29–31] and have been proposed for numerous spaceflight applications [3,17,32–34]. Examples of currently operational ML-based space-based navigation can also be seen in two of NASA's Mars rovers, Perseverance and Curiosity.

Perseverance employs the ML-based navigation software Enhanced AutoNav. It sorts a list of potential paths for the rover to traverse and works with the Approximate Clearance Evaluation (ACE) algorithm to evaluate the safety of ranked paths [35]. To reduce the high computational cost of operating ACE, two heuristics are used to accelerate the path selection process: the Gradient Convolution and Learned Heuristics. Gradient Convolution Heuristic assesses the terrain roughness by analyzing the terrain's gradient. Learned Heuristic predicts the ACE value based on the heightmap data of the terrain. Both heuristics evaluate the local terrain to prioritize optimal paths and reduce the computational cost to the rover.

Curiosity utilizes Autonomous Exploration for Gathering Increased Science (AEGIS), another ML-based system used to autonomously select and prioritize targets for analysis [36]. With AEGIS, Curiosity's Chemistry and Camera instrument can autonomously select target rocks for its laser spectrometer and telescopic camera. It analyzes images from Curiosity's stereo Navigation Camera or ChemCam's Remote Micro-Imager to identify potential targets based on adjustable criteria set by scientists [37].

These examples illustrate the practicality and reliability of ML applications in complex space systems. With sufficient development and training, these techniques have helped improve planetary navigation and streamline robotic operations.

3.2. ARC-LIGHT Prototype Development

3.2.1. Experiment Methodology

We have constructed the Sensor Efficacy in the Lunar Environment Experiment (SELENE), which is a physical test chamber to simulate the optical interference encountered during lunar vertical descent and provide us with training data for prototype algorithm development.

SELENE is composed of a 0.91 × 0.91 × 1.2 m^3 sealed acrylic tank with several mounting points for the sensors, fans, laser, photodiode, and atomizer used to simulate and study this optical environment. Figure 4 shows the layout of the experiment. A 2D scanning lidar and camera are mounted on the underside of the removable lid pointed toward the base of the tank. This is to mimic the nadir-pointing sensors used by landers. A 2D lidar was used for prototype simplicity and budget constraints. A target can be placed at the base of the tank: either a model of the lunar surface for image processing-focused experiments or a series of simple blocks for lidar evaluation. The large scale of the experiment is necessitated by the magnitude of the manufacturer-stated accuracy of our lidar, a Hokuyo UST-10LX (Osaka, Japan), which is ±4 cm. A 650 nm laser is mounted on one wall, pointed to a photodiode on the opposite face to measure optical depth.

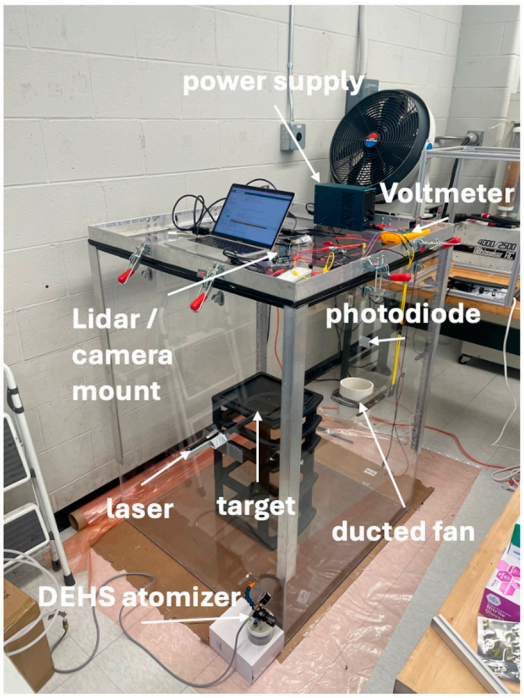


Figure 4. Annotated image of SELENE. The tank is sealed with latches, allowing for the lid to be removed for interior access.

For the initial prototyping of ARC-LIGHT, a Di-Ethyl-Hexl-Sebacate (DEHS) atomizer (Topas GmbH, Dresden, Germany) was used to inject a mist of ~1 micron droplets into the chamber. DEHS is a non-reactive, colorless, odorless substance that can persist for hours as a mist, which we elected to use in place of a lunar regolith simulant due to laboratory protocol restrictions. DEHS is safe for human exposure, although masks are worn at all times during experiments. The fan system circulated the mist around the chamber to establish a homogeneous distribution of particles. The optical depth of the tank, which is assumed to be a linear function of distance through the homogeneous droplet mist, was calculated by measuring the increase in optical extinction of the laser based on the decrease in photodiode voltage as the mist is injected. The experimental constraint of only measuring the optical extinction across one transect through the test chamber drove the

requirement to use a homogenous medium; future work may relax this constraint when multi-point measurements are available.

DEHS droplets have different optical properties than lunar regolith, but since we are focused on understanding the performance of lidars and cameras, the effective cross-section and scattering phase function (SPF) of these particle types are the key parameters to compare. Optical depth characterizes the amount of light extinction through some medium and depends on particle cross-section σ as shown in Equation (1); as such, knowledge of the relative cross-section allows for scaling between DEHS and regolith densities required to achieve the same optical extinction. The SPF describes the probability of light scattering into a given direction. As such, the value of the SPF at 180° represents the backscattering efficiency of the particle. This is important for the lidar, which infers the distance to an obstacle using backscattered light.

Figure 5 shows the dimensionless scattering coefficient $Q_{sc} = \sigma / \pi a^2$ and SPF on the left and right, respectively, for both particle types and four-particle radii a. The DEHS droplets are assumed to be spherical, and their properties were calculated using miepython [38]. The selected particle sizes span the size distribution of regolith [39]. Our lidar operates at 0.9 microns, and the laser-photodiode system operates at 0.65 microns. At these wavelengths, the left panel shows that the effective cross-section of DEHS is typically within ~20% of the regolith cross-section, especially for smaller particles. By contrast, the right panel shows that the backscattering efficiency (i.e., the SPF at large scattering angles) is typically one or two orders of magnitude larger for the DEHS droplets, especially at the lidar wavelength of 0.9 micron. Assuming a comparable single scattering albedo for both regolith and DEHS, DEHS droplets will pose a far more significant obstacle to the lidar than regolith grains would. Their comparable cross-sections mean both will scatter a similar amount of light out of the line of sight, which means their impact on camera images is more comparable.

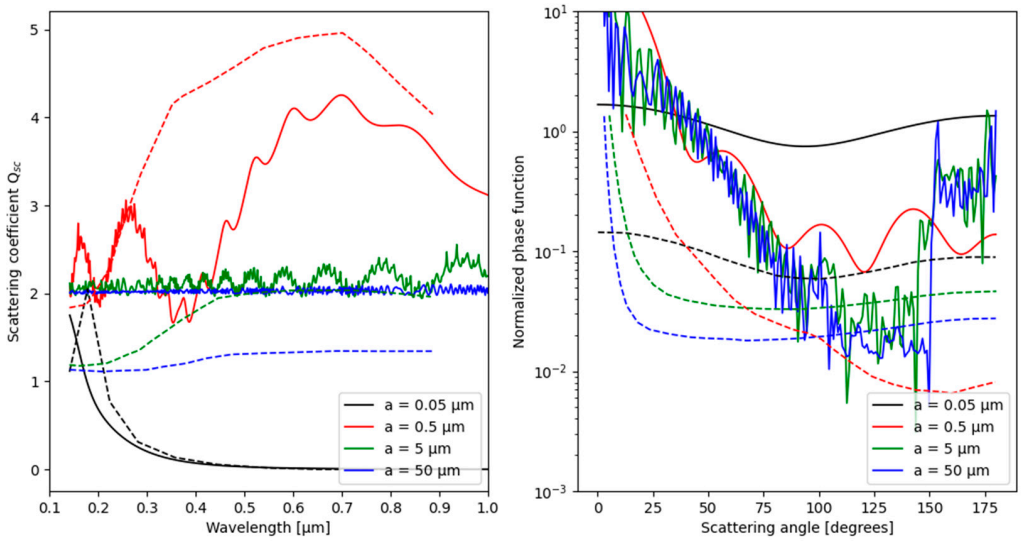


Figure 5. (**a**) Dimensionless scattering coefficients for irregular regolith grains (dashed) and spherical DEHS droplets (solid) of different radii. (**b**) Scattering phase function, normalized to the single scattering albedo, of the same size particles for 0.65 μm wavelength light. Regolith data from [40].

Experiments with SELENE proceed by placing a target of interest in the tank and sealing the lid. The photodiode voltage with the laser incident on it is recorded. Then, DEHS is gradually injected in controlled bursts, with the fan active to thoroughly circulate it. Between each addition of DEHS, a lidar scan, camera image, and photodiode voltage

measurement are gathered and recorded. This process is repeated until the DEHS presents a completely opaque barrier to the lidar, which is the most sensitive to the particles, as discussed above. This occurs around $\tau \approx 0.6$, which is comparable to the optical depth a lander ~10 m above the surface would encounter, assuming a uniform density of $n = 10^9$ particles/m^3 [8]. These experiments allow us to gather sensor data in a controlled setting and independently characterize the amount of interference using the optical depth as a proxy. Figure 6 shows images and lidar scans gathered for a simple square target. The lidar scan maps to the vertical centerline of the image, where X is the position along the tank base and Z is vertical height.

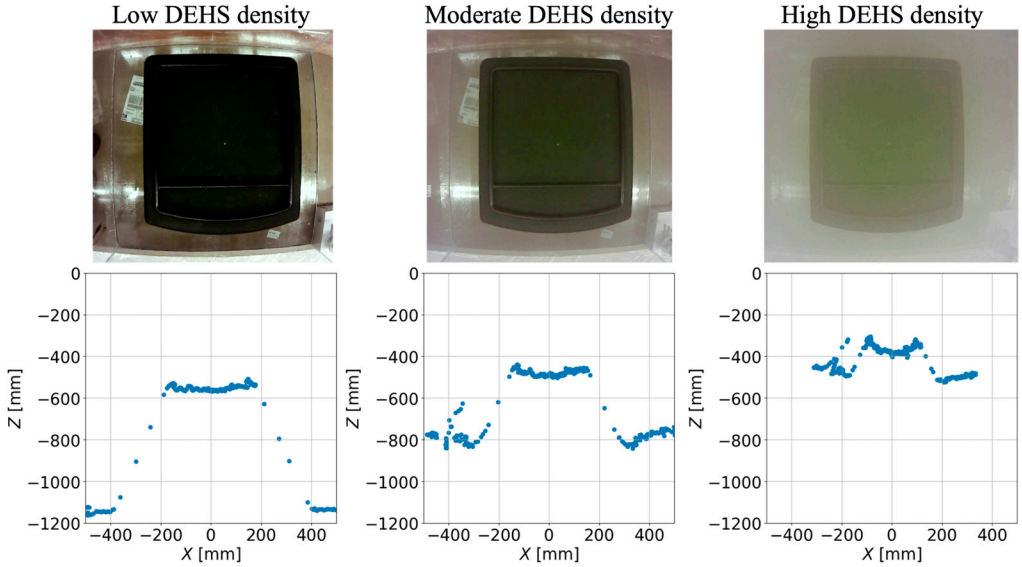


Figure 6. At the top are the example camera images with their respective lidar scans below them from SELENE. DEHS density increases from (left) to (right) panels. The lidar scan crosses the center of the image from top to bottom.

3.2.2. Software Development Methodology

To demonstrate ML-based sensor fusion feasibility and utility in the context of PSI-impacted landings, we have developed a prototype algorithm that fuses data from the camera and lidar to deliver a better data product than either sensor could provide alone. This prototype represents a preliminary version of the optical depth CNN and lidar reconstruction components of the proposed ARC-LIGHT algorithm shown in Figure 2. Our prototype algorithm uses a camera image to estimate the optical depth of the tank, which allows for the attenuated lidar signal to be reprojected as if the measurement were made without any scattering medium present. This is possible because the lidar scan at large optical depths represents a combined signal of the base of the tank and the backscatter from the DEHS. Figure 6 illustrates this. In the middle panel, the lidar is still able to detect the difference between the target and the base of the tank, even though the entire structure is measured to be closer to the lidar located at (0,0). It is hypothesized that knowledge of the optical depth would allow for the lidar scan to be projected back to the distances observed when no DEHS is present, allowing us to "see through" the obstruction.

A training dataset of hundreds of images taken inside SELENE at different DEHS densities, ambient lighting conditions, and arrangement of objects within the camera field of view was used to train the CNN. Critically, the laser-photodiode system allows us to label this dataset according to the measured optical depth. Figure 7 shows the architecture of the CNN; it accepts a 100 × 100 pixel black-and-white image as input and outputs an estimate of the optical depth. A total of 3 hidden layers of 64 nodes (or "neurons") each are used, with rectified linear unit (ReLU) activation functions between each hidden layer. A sigmoid

activation function is used for the last layer, which ensures the output is a value between 0 and 1, spanning the range of optical depths tested. For each training step ("epoch"), the CNN is fed a training image and returns an estimate of the optical depth $\hat{\tau}$. The difference between $\hat{\tau}$ and the true optical depth τ, the "loss", is calculated. The network then "learns" by adjusting the weights and biases of each neuron via backpropagation to minimize the loss. As such, the loss of the CNN decreases as it trains, representing convergence toward a solution.

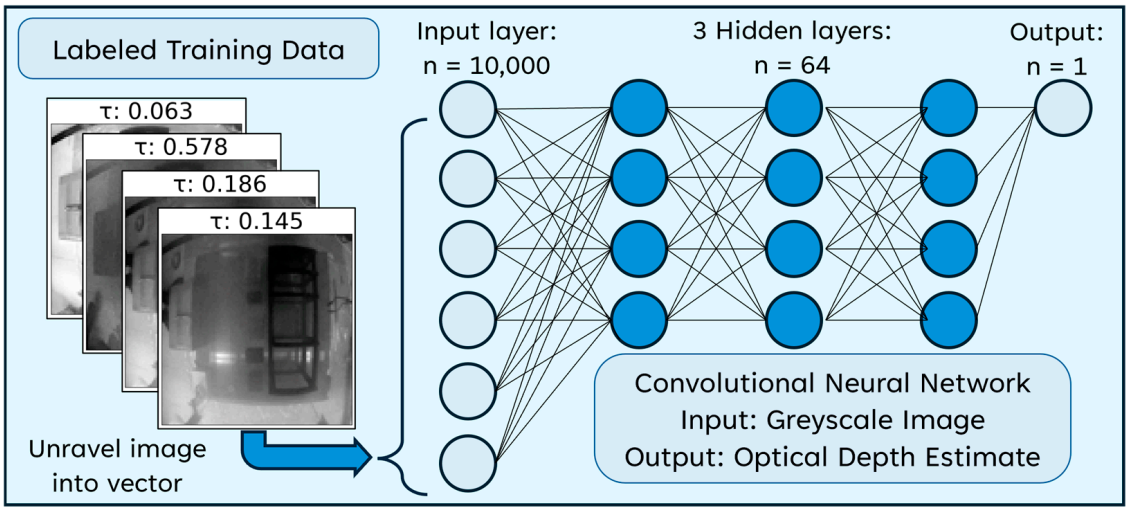


Figure 7. Prototype CNN architecture. The training images with known optical depths are used to train the network, which is composed of multiple layers of n neurons each. For a given image (100 × 100 pixel values), it outputs an estimate of the optical depth (value between 0 and 1).

To quantify training success, 20 random images from the SELENE dataset are reserved for testing its prediction accuracy. The CNN is not trained on these images. Figure 8a,b show the CNN output before and after training, respectively, for these test images, as well as the loss over the training epochs, Figure 8c. The center panel shows that $\hat{\tau}$ successfully converges to τ after training, indicating that the CNN can generalize from its training data and estimate τ for new images. Alongside this, lidar scans at varying optical depths are used to develop an analytic fit for the signal attenuation, $\chi(\theta, \tau)$. χ is defined as the lidar measured distance over the true distance at each scan angle θ and optical depth τ. For this fitting, scans of the flat base of the tank without any obstacles were used for consistency. The solid lines in the left panel of Figure 9 show χ as a function of θ for multiple optical depths, as indicated by the line color; red represents small optical depth, and blue is large optical depth. These curves are each fit to the function:

$$\chi = a\theta + b + \theta^{-c} \tag{3}$$

where a, b, and c are free parameters determined by the fitting. These fits are shown as dashed lines on the left panel of Figure 9. The right panel of Figure 9 shows the values of the free parameters as a function of τ. A second set of functions is fit to these free parameters. Together, this allows for the determination of χ as a function of θ and τ for any new lidar scan. The algorithm thus deploys the CNN to compute $\hat{\tau}$ and uses this output to compute χ at each scan angle θ. Dividing the raw lidar signal by χ gives the projected lidar scan.

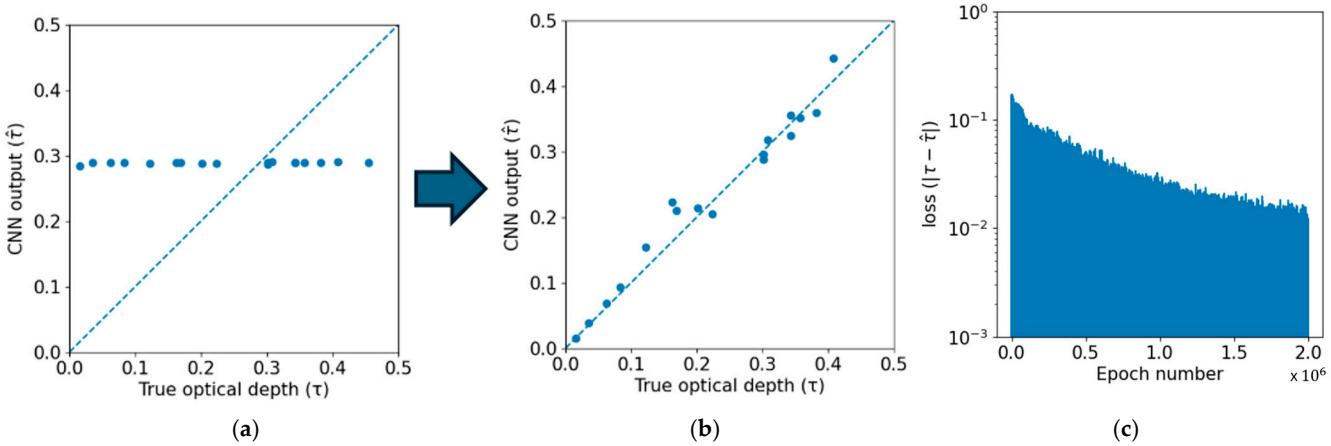


Figure 8. CNN training metrics. (**a**) CNN estimate of the optical depth for the test data, plotted against the true value before training. (**b**) CNN estimate of the optical depth for the test data, plotted against the true value after training completes. (**c**) Plot of CNN loss across the training epochs.

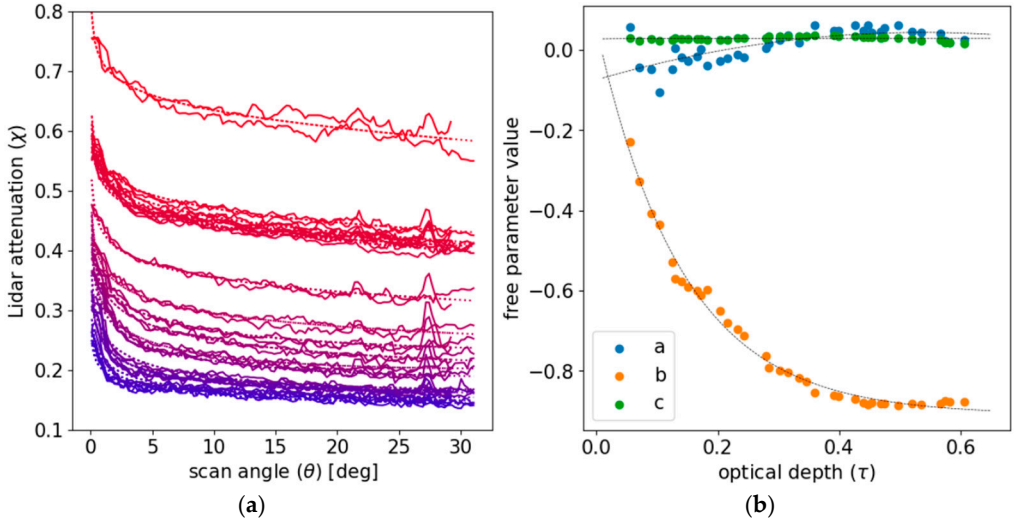


Figure 9. (**a**) Lidar distance attenuation as a function of angle. 0 degrees is looking straight down. Color represents the optical depth of the tank for each scan, ranging from 0 (red) to 0.6 (blue). Solid lines are lidar data; dotted lines are analytic fit. (**b**) Plot of Equation (3) free parameters as a function of τ.

3.3. Prototype Results and Discussion

Figure 10 shows three example lidar reconstructions of SELENE's tank base at different optical depths using this prototype algorithm. The lidar scan corresponds to a slice down the center of the image. In all cases, τ and $\hat{\tau}$ are similar, indicating the CNN successfully estimates the image optical depth. This is to be expected, given the tight agreement shown in the center panel of Figure 8. The right panels of Figure 10 show the associated lidar scans for each image. The raw scan data, shown as the dashed light-blue line, incorrectly measures the tank base to be closer to the lidar than it is. The black dashed line shows the true distance, as measured when no DEHS is present. The solid blue lines show the lidar scan projected using the CNN output $\hat{\tau}$ and the lidar attenuation parametrization χ. In all cases, there is good agreement between the ground truth and the projected lidar scan. This indicates this system can estimate the distance to the tank base even at high optical depths where the lidar scan is significantly impacted by the DEHS.

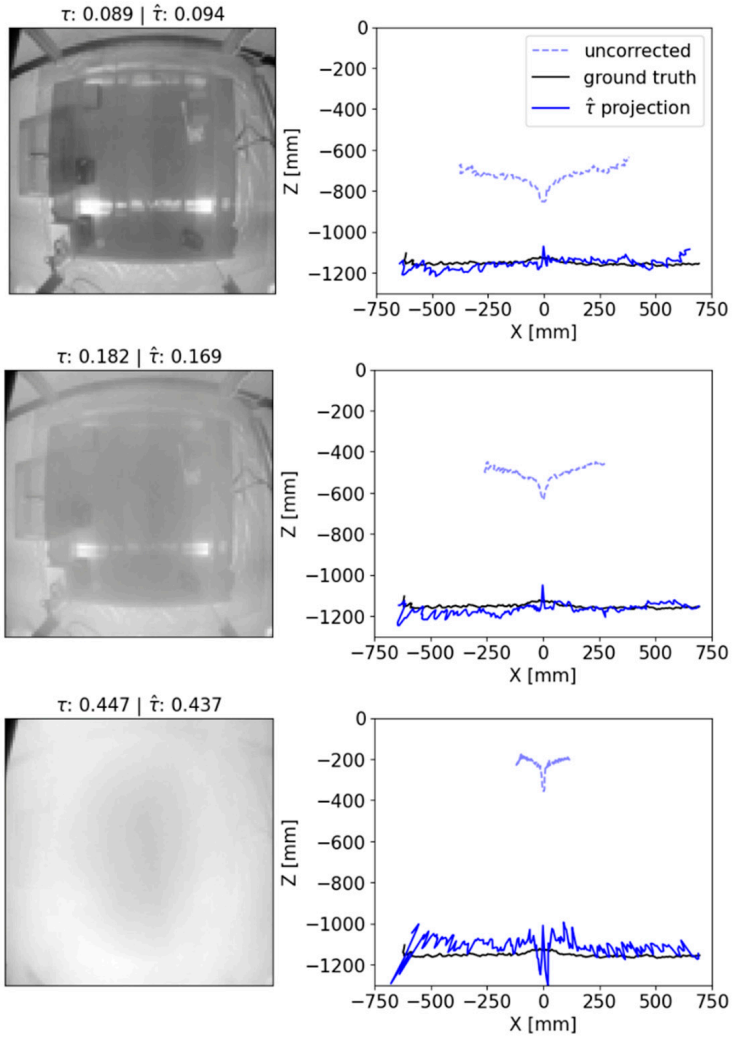


Figure 10. Projections of lidar scans for three DEHS densities. On the left side are the images from SELENE labeled by the measured optical depth (τ) and CNN estimate ($\hat{\tau}$). On the right side are their respective lidar scan, showing the raw lidar scan (dashed blue), ground truth geometry (black solid), and projected lidar scan using $\hat{\tau}$ (blue solid).

These promising results suggest this sensor fusion methodology can provide significant advantages in measuring the distance between the lidar and the target obstacle. Nonetheless, this system relies on multiple limiting assumptions, which could be easily addressed in the near future. Assuming a homogenous DEHS number density, the optical depth can be taken as linearly proportional to the path length. Furthermore, we neglect any differences in path lengths in the camera data, effectively assuming the optical depth to be constant for the whole image. In addition, due to the simple analytic fit used to determine χ, the lidar projection is only reliable for the same geometry it was fit to. Distance estimation error begins to arise when the height of an obstacle is a significant fraction of the distance between the lidar and the target since the tops of these obstacles are therefore at different optical depths. To improve the distance determination in varied, unknown environments, implementing a second CNN to predict χ would remove the limitation of requiring a consistent surface geometry for the lidar projection. Modifying the CNN to subdivide the image and independently predict τ in each sector of the image would also relax the assumption of a constant optical depth and build resilience to spatial and angular inhomogeneity. Constant illumination was used for all experiments to reduce the size of the dataset needed to train the CNN. Expanding the experimental dataset to include a

range of lighting conditions would ensure that optical depth characterization is robust to varied lighting conditions, including the low illumination angles encountered during a lunar south pole landing.

This prototype demonstrates how ARC-LIGHT will fulfill its three objectives. By reconstructing a compromised lidar scan using camera imagery, this system allows for an independent measurement of the sensor's position relative to the surface and the identification of its geometry. As outlined in Section 2.4, this may be used for state vector calibration or IMU redundancy. The proposed addition of a CNN for lidar attenuation estimation will further enhance the system's ability to resolve small surface hazards and help decrease the systematic error near nadir angles. On a technical level, it demonstrates how such a system may operate with comparable computational resources to a lander. For instance, the AiTech SPO-S processor used by the NOVA-C operates at 1 GHz with 1 GB RAM [5]; scaling the computational power of the laptop used to query the CNN to this performance results in acceptable compute times of <1 s.

This prototype marks an important first step to develop ARC-LIGHT for future lunar missions, and we recognize it is just the beginning. Given the positive feasibility assessment results, we took a systems engineering approach to develop the technical management plan needed to execute the remaining phases of ARC-LIGHT development. The proposed timeline, risk analysis, and budget we developed are described in Appendix A.

4. Conclusions and Future Work

NASA's 2024 Human Lander Challenge sought out various university teams to address the complex issue of managing lunar dust. PSI during landing is one of the key challenges future lunar missions will have to address in exploring the lunar surface and establishing a long-term human presence on the Moon. As University of Michigan's team, we proposed a system-level solution, ARC-LIGHT, that could be implemented within a five-year timeline to improve sensor utility during landings affected by PSI. We proposed a ML-based sensor fusion system that integrates sensor data from the cameras, lidars, or radars that landers already carry but disable during the final landing phase. ARC-LIGHT was developed to remove erroneous signals and recover a useful detection of the surface for use by the spacecraft to adjust its descent profile. We developed a prototype algorithm and a purpose-built test bed, SELENE, to gather data and determine the feasibility of ARC-LIGHT. The algorithm was trained on data from SELENE using DEHS droplets. The results from these experiments demonstrated that the sensor fusion methodology developed for ARC-LIGHT can provide significant advantages to see through the particle interference. The information we gained from our initial analysis and prototype is extremely valuable and will help guide us on the next steps of ARC-LIGHT.

Although the DEHS droplets used in our initial testing are particularly effective in backscattering the lidar signal to improve the fidelity of this prototype, experiments with lofted regolith or droplets of a smaller refractive index (and hence a lower backscattering efficiency) would be valuable. Therefore, currently the team at Michigan is working on additional functional testing to ensure ARC-LIGHT can work under lunar conditions. We are upgrading SELENE to better reflect the environmental conditions of a lunar landing, including the use of lunar regolith simulant, varied illumination angles and intensities, and inhomogeneous dust densities. These refinements will get us one step closer to preparing ARC-LIGHT for future lunar missions. We envision ARC-LIGHT being on future missions first in a non-active mode to collect data and verify the system and then to be used as a key tool during the landing process. Adapting ARC-LIGHT to work with lunar simulant will get us one step closer to flight readiness and will be crucial to gain a deeper understanding of PSI processes and aid in the EDL process.

Author Contributions: Conceptualization, A.C. and A.B.; methodology, A.C., A.B., S.C., C.W., J.I.A., M.S., N.G. and Y.G.; software, A.C. and C.W.; formal analysis, A.C.; resources, M.G.; data curation, A.C.; writing—original draft preparation, A.C., A.B., S.C., C.W., J.I.A., M.S. and Y.G.; writing—review and editing, M.G. and C.R.; visualization, A.C.; supervision, M.G. and C.R.; project administration, A.C., A.B. and S.C.; funding acquisition, A.C., A.B. and S.C. All authors have read and agreed to the published version of the manuscript.

Funding: This research was funded by University of Michigan's Space Institute Power Grant. After being selected as finalists for NASA's Human Lander Challenge (HuLC), we received additional funding from NASA HuLC to complete the research.

Data Availability Statement: The raw data supporting the conclusions of this article will be made available by the authors on request.

Acknowledgments: We would also like to acknowledge Nilton Rennó for guidance during the proposal writing and project conceptualization stage.

Conflicts of Interest: The authors declare no conflicts of interest.

Appendix A. Systems Engineering Management Plan

NASA's Human Lander Challenge (HuLC) 2024 asked student teams to develop innovative, system-level solutions to understand, mitigate, and manage the impacts of lunar PSI that can be implemented within 3–5 years. To compete in the challenge, teams were to develop and submit a proposal and video for their technology. Proposals were reviewed, and selected teams advanced as finalists to submit a final technical paper, poster, prototype demonstration, and presentation.

In addition to providing details about the proposed technology we developed, prototyped, verified, and validated, NASA HuLC also required a realistic assessment of the project schedule, milestones, and budget needed to prepare ARC-LIGHT for a lunar mission within a 3–5 year timeline. In this appendix, we present ARC-LIGHT's risk analysis, mission architecture timeline, and budget we developed for the challenge.

Appendix A.1. Risk Analysis

The development and deployment of ARC-LIGHT carries inherent risks. Here, we review the primary risks related to project timeline, budget, and outcomes and discuss measures to mitigate them.

Appendix A.1.1. Algorithm Architecture Revisions

Developing a robust and accurate ML algorithm for PSI mitigation is a complex task. With limited lunar regolith data available, the algorithm might struggle to learn the nuances of PSI phenomena. This could lead to inaccurate performance and an inability to effectively mitigate PSI risks during lunar landings, necessitating significant revisions to the algorithm design, causing delays and exceeding project budgets. Our synthetic data generation approach, which will be developed in parallel to the algorithm architecture, helps to mitigate this risk. By establishing a flexible simulation framework and data generation pipeline, we can modify the training data type to suit any needed changes in the algorithm. Initial trade studies and algorithm prototyping will also help reveal any significant challenges early in the project.

Appendix A.1.2. Algorithm Errors

An inherent challenge stems from the nature of ARC-LIGHT as a CNN. Unlike traditional, rule-based systems designed by humans, neural networks cannot be easily debugged by hand. While extensive training aims to produce the desired outputs, unforeseen behav-

ior or errors might still occur in rare cases. To mitigate this, we will establish safeguards and checks that can override the system's output in such scenarios. Methods that inherently bound the network's outputs may also be used to ensure that problematic outputs are not returned to the GNC. An example of this is our use of a sigmoid activation layer, as described in Section 3.1, which intrinsically bounds the CNN output between 0 and 1.

Appendix A.1.3. Personnel Expertise

Finding qualified personnel with expertise in both ML and spacecraft navigation systems might be challenging. Delays in hiring or a lack of qualified candidates could negatively impact project timelines. The specialized skill set required for this project may necessitate higher salaries or recruitment efforts focused on specific academic or professional backgrounds. To address this challenge, the project prioritizes a modular design for ARC-LIGHT with clear and well-defined interfaces between signal processing modules. This modularity allows specialists in ML and GNC systems to work more independently on their respective components, simplifying the hiring process by making it easier to find qualified candidates with expertise in each specific domain.

Appendix A.1.4. Hardware and Software Integration

Integrating ARC-LIGHT with existing GNC systems could pose compatibility challenges, given the diversity of existing landers developed for Commercial Lunar Payload Services (CLPS), Artemis, and other initiatives. By designing the algorithm output to match the native data format of the lander's sensors, our approach aims to minimize the need for extensive modifications to either ARC-LIGHT or the existing GNC software. We have also allocated a significant margin in our schedule to accommodate any delays in spacecraft integration and testing.

Appendix A.1.5. Testing and Validation

As with all ML systems, large quantities of data are needed for ARC-LIGHT training and testing. Given the paucity of lunar landings, alternate means of gathering this data are required. To address this, the development of this technology would employ a combination of experimental and synthetic data generation. Experimental campaigns using a higher fidelity test bed will help supply realistic scattering data for the cameras and lidars, and extensive synthetic data will cover the broad parameter range of conditions the lander may encounter. Additionally, the performance of ARC-LIGHT integrated into a lander will be thoroughly validated through ground and in-flight testing. Since ARC-LIGHT imposes no additional payload burden, the software can be deployed for its initial flight in a non-active mode to verify the system without adding risk to the landing. This would involve the system performing its sensor fusion calculations without returning output to the GNC, allowing for post-flight verification of outputs before implementing it as a live system for following landings.

Appendix A.1.6. Signal Processing Computation Cost and Reliability

Each signal processing technique employed by the algorithm carries the risk of failing in the lunar environment or demanding a high computational cost. For instance, the two biggest problems with DCP-based dehazing are categorized as obvious and non-obvious failure. Obvious failure is when pixels appear brighter than the ambient light in an image. Non-obvious failure results from pixels being significantly brighter and standing out from their neighboring pixels. Thus, dehazing is difficult in bright environments or in images that are brightly colored or mostly white, such as the Moon.

To rectify obvious failure, pixel minimum can be rescaled to ensure bright surfaces do not occur in the same section of an image as pixel minimum. Non-obvious failure can be mitigated by normalizing the minimum pixel value in a manner that appropriately corresponds to the average haziness observed throughout the scene. This modified DCP also performs significantly faster than the original [41]. Heuristics strategies, such as those discussed in Section 3.1, may also help to improve computational performance to achieve the target cadence.

Appendix A.2. Timeline

The process of ARC-LIGHT development and deployment is divided into three key activities. Development begins by assembling the software and dataset generation teams, defining project requirements, and identifying suitable spaces for software development and test bed operations. Preferably, this location would have an existing "dirty" vacuum chamber, which would allow the use of regolith simulant without threatening sensitive hardware. Several compatible facilities investigating PSI exist, including one at NASA Marshall [42]. The test bed experiment should be designed to reflect PSI on the lunar surface as accurately as possible to provide a realistic optical environment for the cameras and lidars. Our work with SELENE provides a basic template of the key features of this facility. The team working on the test bed will be divided into three subteams, with one for each sensor (camera and lidar) and one for the test bed's structure. At the same time, we also study the available PSI models and develop the software pipeline to run large numbers of simulations over a broad parameter range (as detailed in Section 2.3) and translate them into synthetic sensor data. These tasks are represented in green in Figure A1.

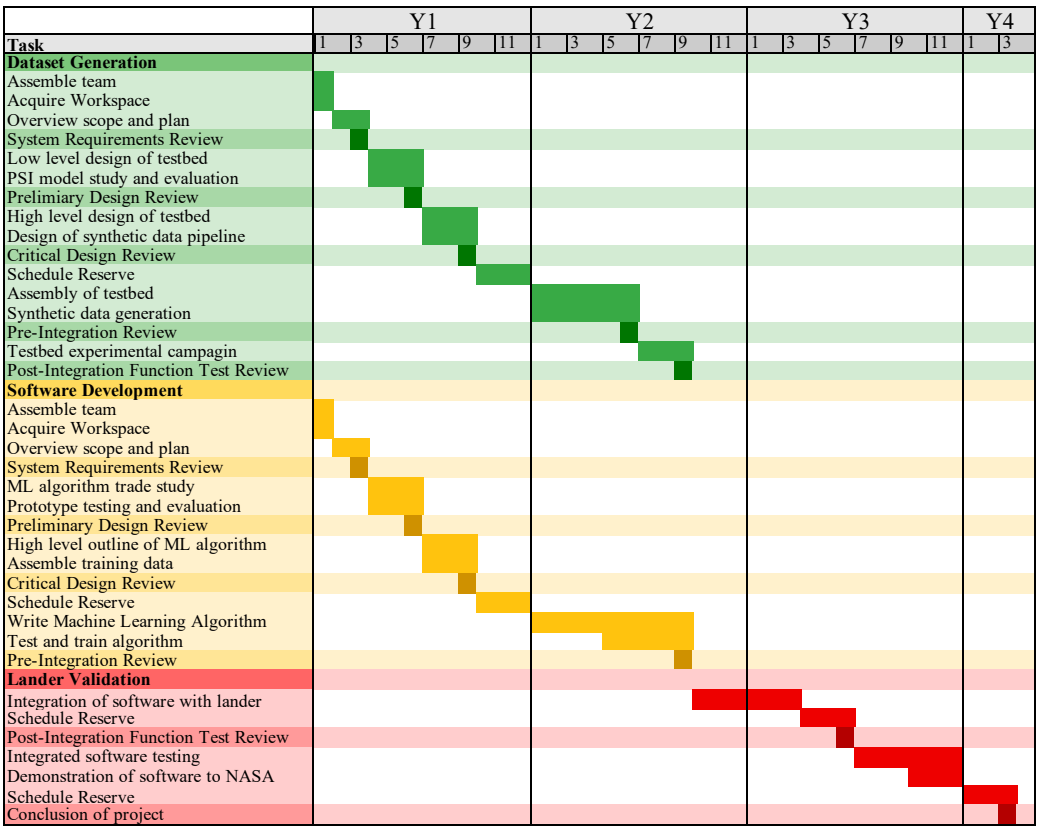


Figure A1. Timeline organized by milestones, year, and month.

The yellow tasks correspond to software development. While the experimental and synthetic datasets are prepared, a team working in parallel begins work on algorithm trade studies, prototyping, and, ultimately, final version development. The team will be further divided into three subteams: one assembling training data, one developing the code, and one verifying the data and the code. This work builds on our prototype development by scrutinizing lander software and hardware constraints to arrive at a more refined algorithm architecture than our candidate design shown in Figure 2 in the main text. The algorithm team will work closely with the test bed and synthetic data teams to ensure the appropriate data is produced for the selected algorithm design. Last, the red tasks encompass integration and testing with the lander. As with all payloads, ARC-LIGHT will be integrated into the spacecraft and tested to ensure successful communication with the spacecraft sensors and GNC. Schedule reserves have been allocated to address any unexpected delays or issues with integration. Once complete, ARC-LIGHT will be ready for flight.

Appendix A.3. Budget

The project requires a total of 15 employees during its 3 ¼ year runtime. The workforce will be divided into six subteams, with the three testbed subteams having a lead engineer, junior engineer, and technician and the three software subteams having a lead engineer and technician. Five of the lead engineers will be needed for the entire project, with an estimated total workload of 780 full-time equivalent (FTE) weeks. The sixth lead engineer will only be needed for 21 months of the project, with an estimated workload of 84 FTE. The 3 junior engineers are needed for 21 months of the project, with an estimated total workload of 252 FTE. The 6 technicians are only needed for 18 months of the project, with an estimated total workload of 432 FTE. The total estimated cost for the combined workload of the workforce required for this project is 1548 FTE.

To develop the high-fidelity lunar test bed, several hardware items are required. The vacuum chamber structure is estimated to cost $150,000; the sensors have $6900 allocated to them, the small rocket thruster is estimated to cost $50,000, and the regolith simulant will cost $3250. A total of $10,000 has been allocated for extra hardware that may be required for the project. The total estimated cost for the hardware used for this project is $220,150. These costs could be reduced if a suitable existing vacuum chamber can be accessed.

High-grade computers will be necessary for the creation of the ARC-LIGHT software. Four computers would most likely be needed, totaling an estimated $20,000. Three years of cloud computing access would be necessary for conducting the PSI simulations for synthetic data generation and CNN training, totaling an estimated $30,000. A total of $5000 has been allocated for any additional software costs. The total estimated cost for the software development is $55,000. The combined estimated cost of the ARC-LIGHT project is shown in Figure A2, which includes $275,150 in hardware and software costs plus 1548 FTE weeks of salary costs, approximately amounting to $3.3 M dependent on salary costs.

Category	Cost				Notes
	Number	Unit	Unit Cost	Final Cost	
A. Salaries			(FTE Weeks)	(FTE Weeks)	
Lead Engineers	5	Employees	156	780	Needed for duration of project
Lead Engineer (Training Data subteam)	1	Employees	84	84	Only needed until testbed is finished with assembly
Junior Engineers	3	Employees	84	252	
Technicians	6	Employees	72	432	Hired at the beginning of PDR, and only needed until testbed is finished with assembly
Salaries Total				**1548**	
B. Hardware			($)	($)	
Lidar	3	N/A	$2000	$6000	One for prototyping, one for testing, one for backup
Camera	3	N/A	$300	$900	
Radar	3	N/A	$2000	$6000	
Thruster	1	N/A	$50,000	$50,000	Replicates thruster on lander
Testbed & Vacuum Chamber Structure	1	N/A	$150,000	$150,000	Contains experiment
Regolith Simulant	50	Kg	$65	$3250	Propelled by thruster
Additional Hardware	1	N/A	$10,000	$10,000	Additional equipment needed for assembly and testing
Hardware Total				**$226,150**	
C. Software					
Computers	4	N/A	$5000	$20000	Needed to create ML algorithm and run tests
Cloud Space	3	Years	$10,000	$30,000	Storage Space and Power
Additional Software	1	N/A	$5000	$5000	Additional software needed to create algorithm
Software Total				**$55,000**	

Total Cost	FTE	Dollars
	1548	**$281,150**

Figure A2. Budget estimating the total cost of the development of ARC-LIGHT.

References

1. McDivitt, J. *Apollo 15 Mission Report*; Technical Report; NASA Manned Spacecraft Center: Houston, TX, USA, 1971.
2. Li, S.; Jiang, X.; Tao, T. Guidance summary and assessment of the Chang'e-3 powered descent and landing. *J. Spacecr. Rocket.* **2016**, *53*, 258–277. [CrossRef]
3. Ghilardi, L.; Furfaro, R. Image-Based Lunar Hazard Detection in Low Illumination Simulated Conditions via Vision Transformers. *Sensors* **2023**, *23*, 7844. [CrossRef]
4. Zhang, H.; Li, J.; Wang, Z.; Guan, Y. Guidance Navigation and Control for Chang'E-5 Powered Descent. *Space Sci. Technol.* **2021**, *2021*, 9823609. [CrossRef]
5. Getchius, J.; Renshaw, D.; Posada, D.; Henderson, T.; Hong, L.; Ge, S.; Molina, G. Hazard Detection and Avoidance for the Nova-C Lander. *arXiv* **2022**, arXiv:2204.00660.
6. JAXA. SLIM Project Press Kit. 2024. Available online: https://global.jaxa.jp/countdown/slim/SLIM-mediakit-EN_2310.pdf (accessed on 5 June 2024).
7. China National Space Administration. China's Chang'e-6 Lands on Moon's Far Side to Collect Samples. 2024. Available online: https://english.www.gov.cn/news/202406/02/content_WS665bc29ec6d0868f4e8e7c54.html (accessed on 30 January 2025).
8. McDivitt, J. *Apollo 12 Mission Report*; Technical Report March; NASA Manned Spacecraft Center: Houston, TX, USA, 1970.
9. Immer, C.; Lane, J.; Metzger, P.; Clements, S. Apollo video photogrammetry estimation of plume impingement effects. *Icarus* **2011**, *214*, 46–52. [CrossRef]
10. Zhong, H.; Wang, H.; Wu, Z.; Zhang, C.; Zheng, Y.; Tang, T. A survey of LiDAR and camera fusion enhancement. *Procedia Comput. Sci.* **2021**, *183*, 579–588. [CrossRef]
11. Yusefi, A.; Durdu, A.; Toy, I. Camera/LiDAR Sensor Fusion-based Autonomous Navigation. In Proceedings of the 2024 23rd International Symposium INFOTEH-JAHORINA, East Sarajevo, Bosnia and Herzegovina, 20–22 March 2024. [CrossRef]
12. Parsons, T.; Sheikhha, F.H.; Seo, J.; Lee, H. RGB-LiDAR sensor fusion for dust de-filtering in autonomous excavation applications. *Autom. Constr.* **2024**, *168*, 105850. [CrossRef]
13. Afzalaghaeinaeini, A.; Seo, J.; Lee, D.; Lee, H. Design of Dust-Filtering Algorithms for LiDAR Sensors Using Intensity and Range Information in Off-Road Vehicles. *Sensors* **2022**, *22*, 4051. [CrossRef] [PubMed]
14. Mirshekarian, S.; Sormaz, D. Machine Learning Approaches to Learning Heuristics for Combinatorial Optimization Problems. *Procedia Manuf.* **2018**, *17*, 102–109. [CrossRef]
15. Horton, M. How to Easily Estimate Vehicle Localization Errors from IMU Specs, March 2023. Available online: https://medium.com/anello-photonics/how-to-easily-estimate-vehicle-localization-errors-from-imu-specs-31e6174ff065 (accessed on 5 June 2024).

16. Honeywell. Compare Our Inertial Measurement Units. Available online: https://aerospace.honeywell.com/us/en/products-and-services/product/hardware-and-systems/sensors/inertial-measurement-units (accessed on 5 June 2024).
17. Song, J.; Rondao, D.; Aouf, N. Deep learning-based spacecraft relative navigation methods: A survey. *Acta Astronaut.* **2022**, *191*, 22–40. [CrossRef]
18. Fontes, D.; Mantovani, J.G.; Metzger, P. Numerical estimations of lunar regolith trajectories and damage potential due to rocket plumes. *Acta Astronaut.* **2022**, *195*, 169–182. [CrossRef]
19. Lane, J.E.; Metzger, P.T. Ballistics Model for Particles on a Horizontal Plane in a Vacuum Propelled by a Vertically Impinging Gas Jet. *Part. Sci. Technol.* **2012**, *30*, 196–208. [CrossRef]
20. Liever, P.; Tosh, A.; Arslanbekov, R.; Habchi, S. Modeling of Rocket Plume Impingement Flow and Debris Transport in Lunar Environment. In Proceedings of the 50th AIAA Aerospace Sciences Meeting including the New Horizons Forum and Aerospace Exposition, Nashville, TN, USA, 9–12 January 2012. [CrossRef]
21. Morris, A.B.; Goldstein, D.B.; Varghese, P.L.; Trafton, L.M. Approach for Modeling Rocket Plume Impingement and Dust Dispersal on the Moon. *J. Spacecr. Rocket.* **2015**, *52*, 362–374. [CrossRef]
22. He, X.; He, B.; Cai, G. Simulation of rocket plume and lunar dust using DSMC method. *Acta Astronaut.* **2012**, *70*, 100–111. [CrossRef]
23. Li, Y.; Ren, D.; Bo, Z.; Huang, W.; Ye, Q.; Cui, Y. Gas-particle two-way coupled method for simulating the interaction between a rocket plume and lunar dust. *Acta Astronaut.* **2019**, *157*, 123–133. [CrossRef]
24. Chinnappan, A.K.; Kumar, R.; Arghode, V.K. Modeling of dusty gas flows due to plume impingement on a lunar surface. *Phys. Fluids* **2021**, *33*, 053307. [CrossRef]
25. Tang, H.; Jia, K. A New Benchmark: On the Utility of Synthetic Data with Blender for Bare Supervised Learning and Downstream Domain Adaptation. In Proceedings of the IEEE Computer Society Conference on Computer Vision and Pattern Recognition, Vancouver, BC, Canada, 17–24 June 2023; pp. 15954–15964, ISBN 9798350301298. [CrossRef]
26. Roberts, M.; Ramapuram, J.; Ranjan, A.; Kumar, A.; Bautista, M.A.; Paczan, N.; Webb, R.; Apple, J.M.S. Hypersim: A Photorealistic Synthetic Dataset for Holistic Indoor Scene Understanding. In Proceedings of the International Conference on Computer Vision, Montreal, QC, Canada, 10–17 October 2021; pp. 10892–10902. [CrossRef]
27. Kandel, I.; Castelli, M. How deeply to fine-tune a convolutional neural network: A case study using a histopathology dataset. *Appl. Sci.* **2020**, *10*, 3359. [CrossRef]
28. Cayamcela, M.E.M.; Lim, W. Fine-tuning a pre-trained Convolutional Neural Network Model to translate American Sign Language in Real-time. In Proceedings of the 2019 International Conference on Computing, Networking and Communications, ICNC, Honolulu, HI, USA, 18–21 February 2019; pp. 100–104, ISBN 9781538692233. [CrossRef]
29. Liu, H.; Wu, C.; Wang, H. Real time object detection using LiDAR and camera fusion for autonomous driving. *Sci. Rep.* **2023**, *13*, 8056. [CrossRef] [PubMed]
30. Xie, G.; Zhang, J.; Tang, J.; Zhao, H.; Sun, N.; Hu, M. Obstacle detection based on depth fusion of lidar and radar in challenging conditions. *Ind. Robot* **2021**, *48*, 792–802. [CrossRef]
31. Huang, L.; Barth, M. Tightly-coupled LIDAR and computer vision integration for vehicle detection. In Proceedings of the IEEE Intelligent Vehicles Symposium, Proceedings. Xi'an, China, 3–5 June 2009; pp. 604–609, ISBN 9781424435043. [CrossRef]
32. Chekakta, Z.; Zenati, A.; Aouf, N.; Dubois-Matra, O. Robust deep learning LiDAR-based pose estimation for autonomous space landers. *Acta Astronaut.* **2022**, *201*, 59–74. [CrossRef]
33. Ohira, G.; Kashioka, S.; Takao, Y.; Iyota, T.; Tsuda, Y. Autonomous image-based navigation using vector code correlation algorithm for distant small body exploration. *Acta Astronaut.* **2022**, *196*, 400–413. [CrossRef]
34. Linares, R.; Campbell, T.; Furfaro, R.; Gaylor, D.E. A Deep Learning Approach for Optical Autonomous Planetary Relative Terrain Navigation. Technical Report. 2017. Available online: https://www.researchgate.net/publication/321534448 (accessed on 5 June 2024).
35. Abcouwer, N.; Daftry, S.; Venkatraman, S.; del Sesto, T.; Toupet, O.; Lanka, R.; Song, J.; Yue, Y.; Ono, M. Machine Learning Based Path Planning for Improved Rover Navigation. In Proceedings of the 2021 IEEE Aerospace Conference, Big Sky, MT, USA, 6–13 March 2021; Available online: https://hdl.handle.net/2014/54255 (accessed on 5 June 2024).
36. JPL. Under Their Own AEGIS, December 2009. Available online: https://scienceandtechnology.jpl.nasa.gov/under-their-own-aegis (accessed on 5 June 2024).
37. Webster, G.; Brown, D.; Cantillo, L. NASA Mars Rover Can Choose Laser Targets on Its Own, July 2016. Available online: https://www.jpl.nasa.gov/news/nasa-mars-rover-can-choose-laser-targets-on-its-own (accessed on 5 June 2024).
38. Prahl, S. miepython: Pure python calculation of Mie scattering. 2024. Available online: https://zenodo.org/records/11135148 (accessed on 7 February 2025).
39. NASA. Cross-Program Design Specification for Natural Environments. Technical Report. 2019. Available online: https://ntrs.nasa.gov/citations/20200000867 (accessed on 5 June 2024).

40. Lolachi, R.; Glenar, D.A.; Stubbs, T.J. Optical monitoring of the dust environment at lunar surface exploration sites. *Planet. Space Sci.* **2023**, *234*, 105709. [CrossRef]
41. Riaz, I.; Fan, X.; Shin, H. Single image dehazing with bright object handling. *IET Comput. Vis.* **2016**, *10*, 817–827. [CrossRef]
42. Diaz-Lopez, M.X.; Gorman, M.; Rubio, J.S.; Ni, R. Plume-surface Interaction Physics Focused Ground Test 1: Diagnostics and Preliminary Results. In Proceedings of the AIAA SCITECH 2022 Forum, Virtual, 3–7 January 2022. [CrossRef]

Disclaimer/Publisher's Note: The statements, opinions and data contained in all publications are solely those of the individual author(s) and contributor(s) and not of MDPI and/or the editor(s). MDPI and/or the editor(s) disclaim responsibility for any injury to people or property resulting from any ideas, methods, instructions or products referred to in the content.